Chandra Gratings Observations of the Focused Wind in Cygnus X-1/HDE 226868

M. Hanke[1,2] – J. Wilms[1,2] – M.A. Nowak[3] – K. Pottschmidt[4,5,6]
N.S. Schulz[3] – J.C. Lee[7] – J. Xiang[7] – A. Juett[5]

[1] Dr. Karl Remeis-Observatory, University of Erlangen-Nuremberg, Bamberg, Germany; Manfred.Hanke / Joern.Wilms @sternwarte.uni-erlangen.de
[2] Erlangen Centre for Astroparticle Physics, University of Erlangen-Nuremberg, Erlangen, Germany
[3] Kavli Institute for Astrophysics and Space Research, MIT-CXC, Cambridge, MA, USA, [4] CRESST, University of Maryland Baltimore County, Baltimore, MD, USA
[5] NASA Goddard Space Flight Center, Greenbelt, MD, USA, [6] Center for Astrophysics and Space Sciences, University of California at San Diego, La Jolla, CA, USA
[7] Harvard-Smithsonian Center for Astrophysics, Cambridge, MA, USA

Abstract

We present results from a 50 ksec observation of the hard state of the supergiant X-ray binary system Cygnus X-1/HDE 226868 with *Chandra*'s High Energy Transmission Grating Spectrometer and simultaneous *RXTE* data. Performed during superior conjunction of the black hole, the observation is ideally suited for spectroscopy of the focused stellar wind in the system. A large number of absorption lines is detected in the X-ray spectrum.

Full results are presented by Hanke et al. (2008, ApJ, submitted).

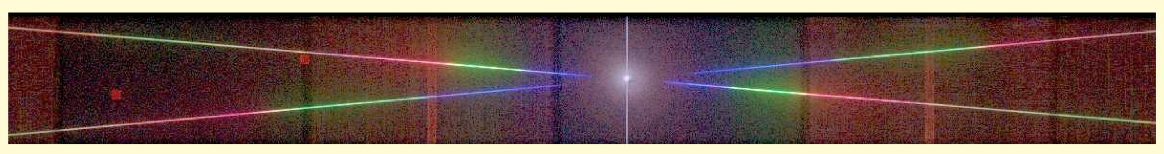

Dispersed image of the *Chandra*-observation. Note the dust scattering halo around the source. The small black square is the zero-order blocking filter applied during the observation.

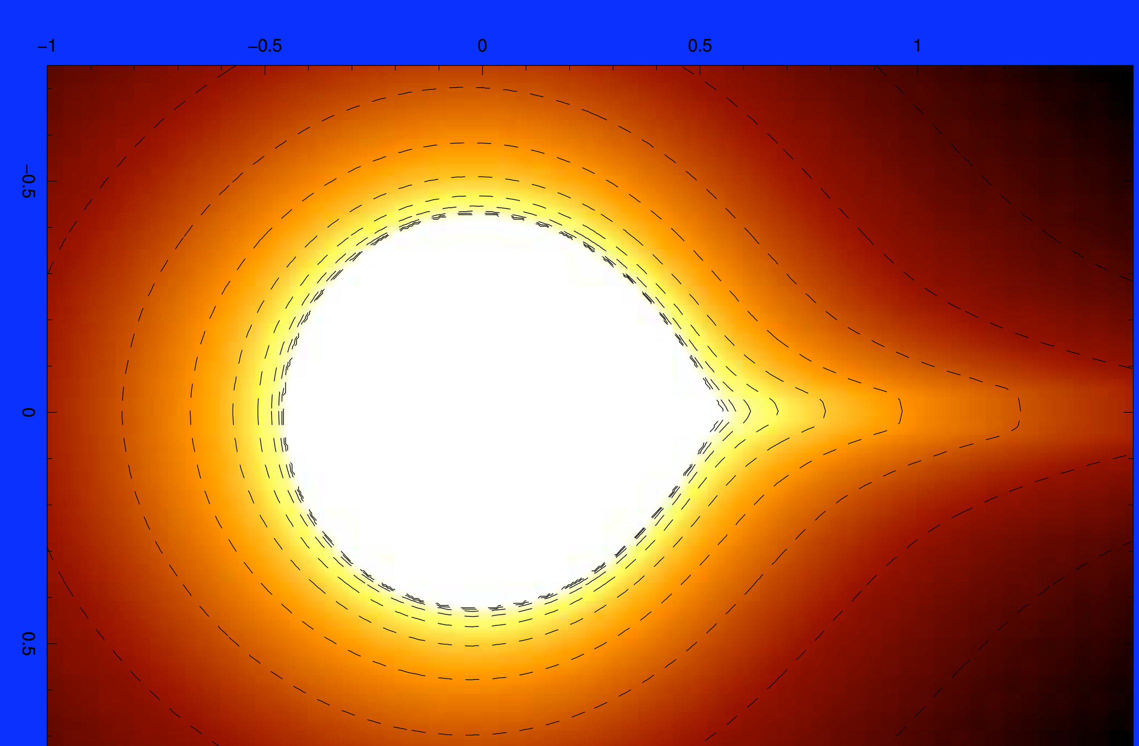

Density distribution in the focused stellar wind of HDE 226868 using the model of Friend & Castor (1982). Distances are measured in units of the binary separation

Introduction

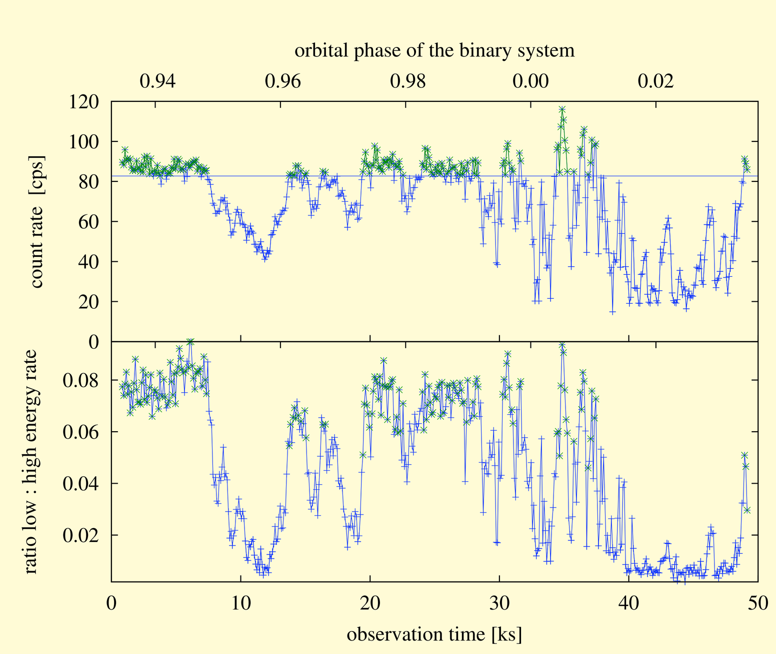

Strong dipping behavior is seen during the observation, due to the focused stellar wind passing through the line of sight. Here, only data taken outside of dips are discussed.

Introduction

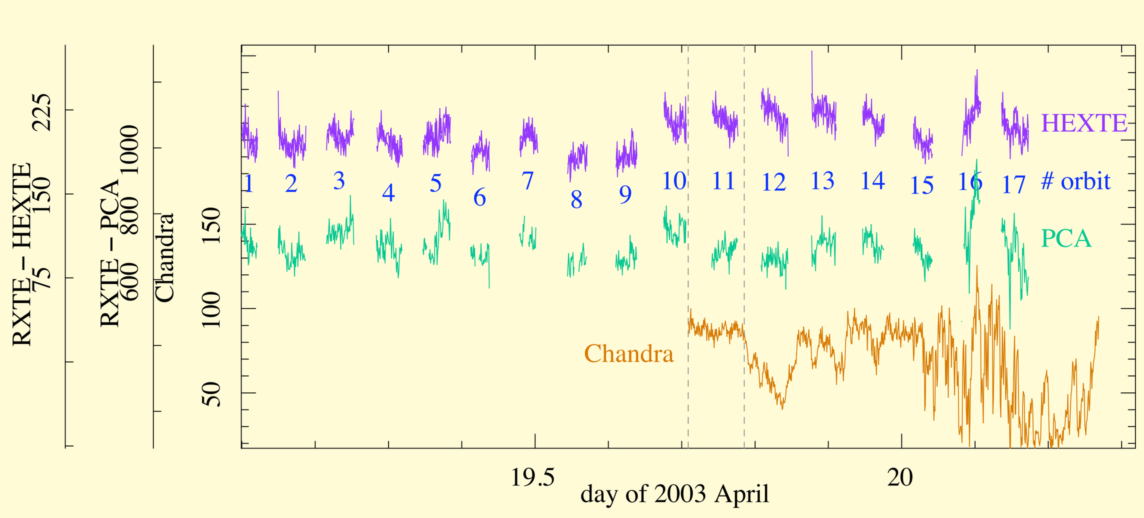

Quasi-simultaneous *RXTE* data show that the dipping probably started before the *Chandra* observation, however, the strongest dipping episodes happened during the simultaneous observation.

Absorption Edges, I

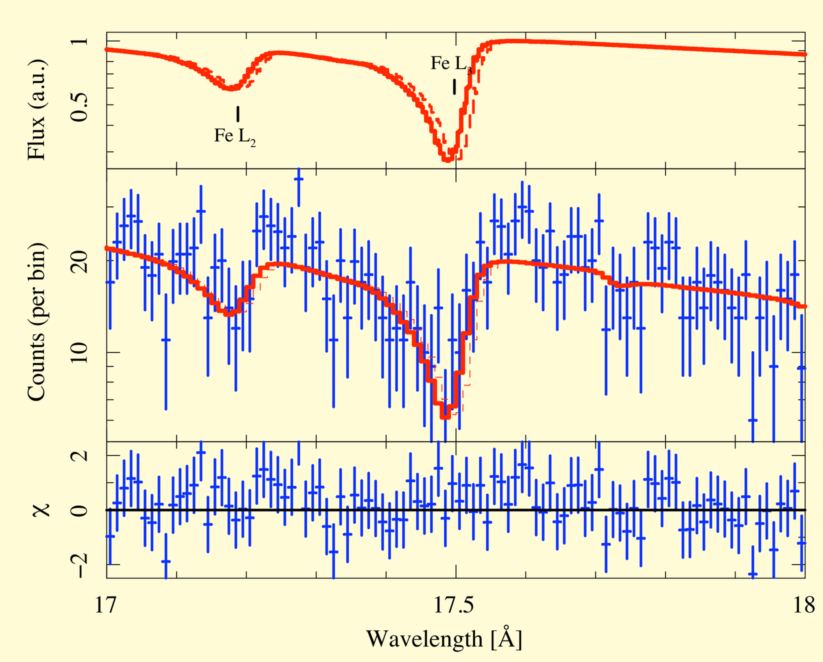

The Fe L_2 and L_3 edges are slightly shifted with respect to their laboratory wavelengths (laboratory indicated by dotted lines): a blueshifted absorber ($v \sim 212\,\mathrm{km\,s^{-1}}$), or chemical shift?

Due to the low SNR in the other edges, all edge energies are compatible with the redshift measured in Fe L, thus the interpretation as a Doppler shift cannot be ruled out.

Absorption Edges, II

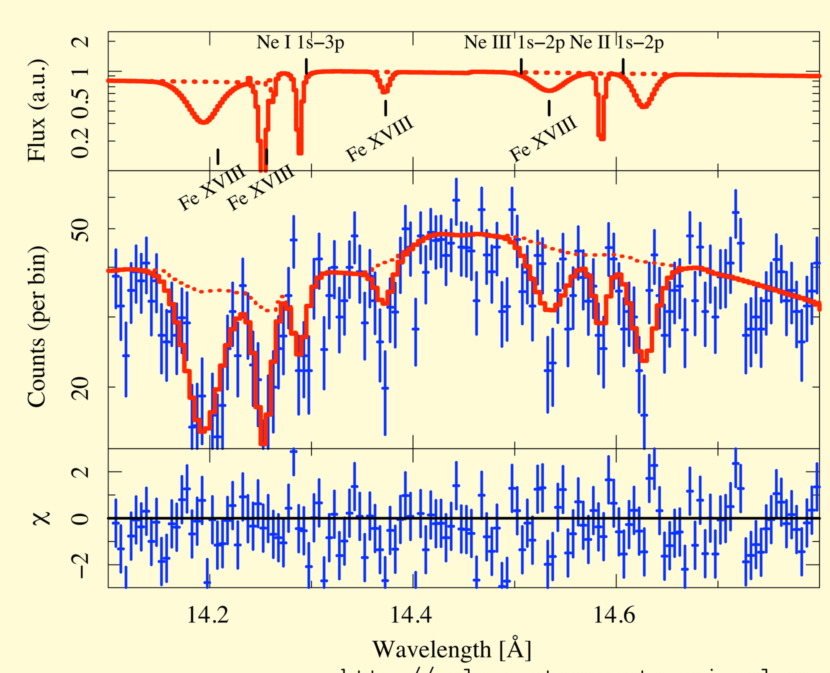

The Ne edge is strongly blended with Fe absorption lines. Note the Ne Kβ line (Ne 1s → 3p), which is due to resonant absorption.

An updated version of the `tbabs` absorption model (Wilms, Allen, McCray) that includes the fine structure of the edges used for the modeling presented here is available at
`http://pulsar.sternwarte.uni-erlangen.de/wilms/research/tbabs.`

Absorption Edges, III

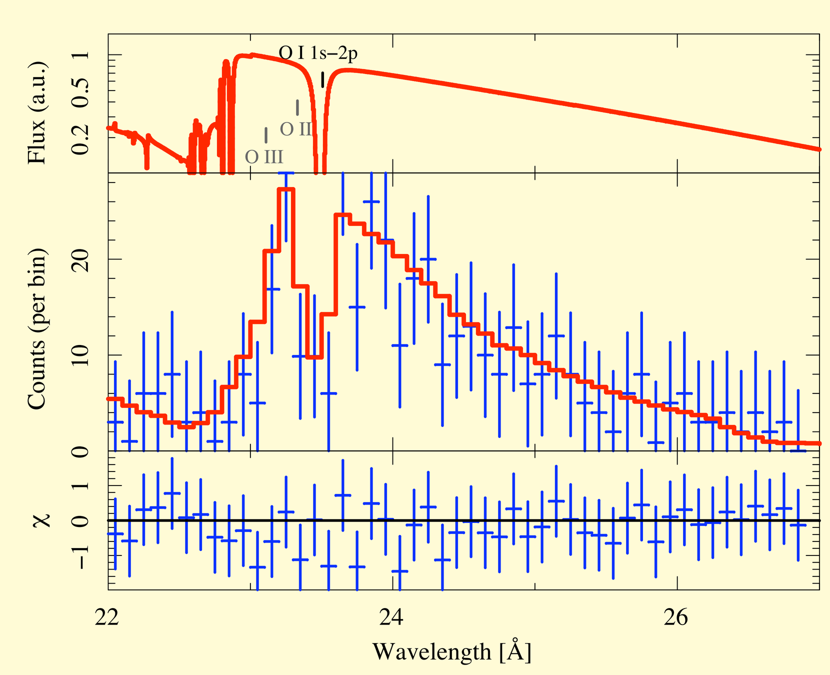

O edge, with the strong O Kα resonance absorption line.

Line Analysis, I

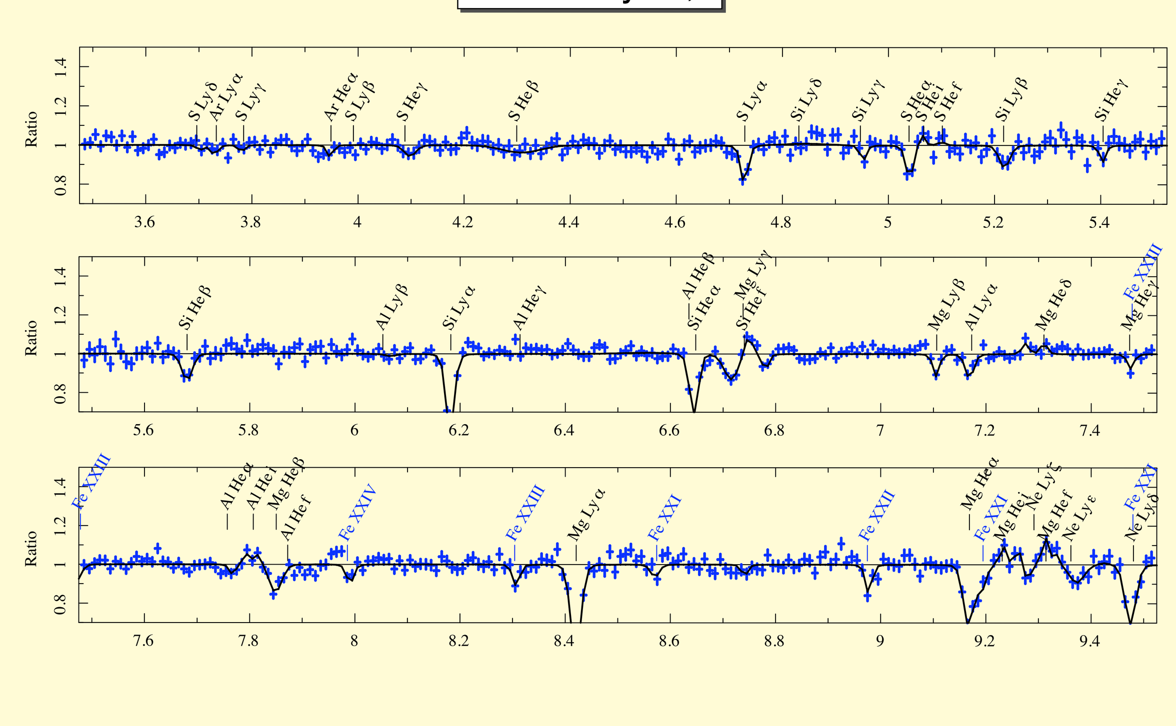

Line Analysis, II

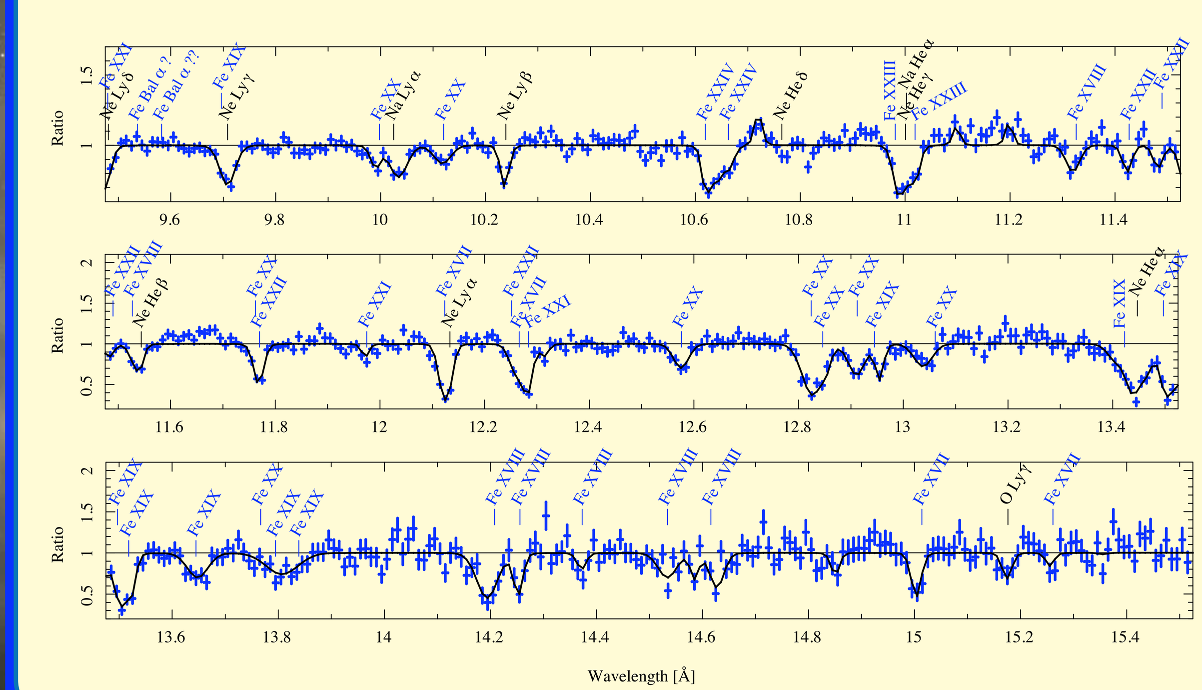

Line Analysis, III

Overview on the detected lines from H- and He-like ions: wavelength in Å

	transition hydrogen-like (1 electron)	O VIII	Ne X	Na XI	Mg XII	Al XIII	Si XIV	S XVI	Ar XVIII	Ca XX	Fe XXVI	Ni XXVIII
Ly α	$1s\,(^2S_{1/2}) \rightarrow 2p\,(^2P_{3/2,1/2})$	18.97	**12.13**	**10.03**	**8.42**	**7.17**	**6.18**	**4.73**	**3.73**	**3.02**	(1.78)	**1.53**
Ly β	$1s\,(^2S_{1/2}) \rightarrow 3p\,(^2P_{3/2,1/2})$	**16.01**	**10.24**	8.46	**7.11**	6.05	**5.22**	3.99	**3.15**	(2.55)	1.50	1.29
Ly γ	$1s\,(^2S_{1/2}) \rightarrow 4p\,(^2P_{3/2,1/2})$	**15.18**	**9.71**	8.02	(6.74)	(5.74)	**4.95**	3.78	**2.99**	2.42	1.43	**1.23**
Ly δ	$1s\,(^2S_{1/2}) \rightarrow 5p\,(^2P_{3/2,1/2})$	(14.82)	**9.48**	7.83	(6.58)	(5.60)	(4.83)	**3.70**	(2.92)	(2.36)	(1.39)	(1.20)
Ly ϵ	$1s\,(^2S_{1/2}) \rightarrow 6p\,(^2P_{3/2,1/2})$	(14.63)	**9.36**	(7.73)	(6.50)	(5.53)	(4.77)	(3.65)	(2.88)	(2.33)	(1.37)	
Ly ζ	$1s\,(^2S_{1/2}) \rightarrow 7p\,(^2P_{3/2,1/2})$	(14.52)	9.29	(7.68)	(6.45)	(5.49)	(4.73)	(3.62)	(2.86)	(2.31)	(1.36)	
Ly η	$1s\,(^2S_{1/2}) \rightarrow 8p\,(^2P_{3/2,1/2})$	(14.45)	9.25	(7.64)	(6.42)	(5.47)	(4.71)	(3.60)	(2.85)	(2.30)	(1.36)	
Ly θ	$1s\,(^2S_{1/2}) \rightarrow 9p\,(^2P_{3/2,1/2})$	(14.41)	(9.22)	(7.61)	(6.40)	(5.45)	(4.70)	(3.59)	(2.84)	(2.29)	(1.35)	

	transition helium-like (2 electrons)	O VII	Ne IX	Na X	Mg XI	Al XII	Si XIII	S XV	Ar XVII	Ca XIX	Fe XXV	Ni XXVII
f [em.]	$1s^2\,(^1S_0) \leftarrow 1s2s\,(^3S_1)$	[22.10]	(13.70)	11.19	**9.31**	**7.87**	**6.74**	5.10	(3.99)	(3.21)	(1.87)	
i [em.]	$1s^2\,(^1S_0) \leftarrow 1s2p\,(^3P_{1,2})$	[21.80]	(13.55)	11.08	**9.23**	**7.81**	(6.69)	5.07	3.97	**3.19**	(1.86)	1.60
r ≡ He α	$1s^2\,(^1S_0) \rightarrow 1s2p\,(^1P_1)$	[21.60]	**13.45**	**11.00**	**9.17**	**7.76**	**6.65**	**5.04**	**3.95**	**3.18**	**1.85**	1.59
He β	$1s^2\,(^1S_0) \rightarrow 1s3p\,(^1P_1)$	18.63	**11.54**	9.43	**7.85**	**6.64**	**5.68**	4.30	**3.37**	**2.71**	1.57	(1.35)
He γ	$1s^2\,(^1S_0) \rightarrow 1s4p\,(^1P_1)$	(17.77)	**11.00**	8.98	**7.47**	6.31	**5.40**	**4.09**	**3.20**	(2.57)	1.50	(1.28)
He δ	$1s^2\,(^1S_0) \rightarrow 1s5p\,(^1P_1)$	(17.40)	10.77	8.79	7.31	(6.18)	(5.29)	4.00	(3.13)	(2.51)	1.46	(1.25)
He ϵ	$1s^2\,(^1S_0) \rightarrow 1s6p\,(^1P_1)$	(17.20)	**10.64**	(8.69)	(7.22)	(6.10)	5.22	3.95	(3.10)			
He ζ	$1s^2\,(^1S_0) \rightarrow 1s7p\,(^1P_1)$	(17.09)	10.56	(8.63)	(7.17)	(6.06)	(5.19)	(3.92)				
He η	$1s^2\,(^1S_0) \rightarrow 1s8p\,(^1P_1)$	(17.01)	(10.51)	(8.59)	(7.14)	(6.03)	(5.16)	(3.90)				

Wavelengths in [square brackets] are not covered by the data, and lines with wavelengths in (parentheses) are not detected, while lines indicated with **bold** wavelengths are clearly detected in our *Chandra*-HETGS observation of Cyg X-1. The wavelengths are taken from the CXC atomic database ATOMDB and the table of Verner et al. (1996).

Line Analysis, IV

Fit results for the absorption line series

ion	N(ion) [$10^{16}\,\mathrm{cm^{-2}}$]	$c\cdot\Delta\lambda/\lambda$ [$\mathrm{km\,s^{-1}}$]	ξ_0 [$\mathrm{km\,s^{-1}}$]
Ne X	31^{+15}_{-9}	-87^{+21}_{-26}	38^{+8}_{-7}
Ne IX	$2.6^{+0.9}_{-0.7}$	-151^{+39}_{-42}	159^{+99}_{-66}
Na XI	$1.2^{+0.4}_{-0.4}$	200^{+139}_{-127}	306^{+152}_{-146}
Na X	$0.7^{+0.2}_{-0.3}$	-11^{+116}_{-122}	287^{+158}_{-190}
Mg XII	$6.1^{+1.0}_{-0.3}$	-28^{+29}_{-29}	211^{+64}_{-68}
Mg XI	4^{+2}_{-1}	-55^{+23}_{-39}	60^{+14}_{-13}
Al XIII	5^{+10}_{-4}	-133^{+65}_{-170}	9^{+401}_{-9}
Al XII	$0.7^{+2.3}_{-0.6}$	-67^{+243}_{-125}	11^{+799}_{-11}
Si XIV	$9.8^{+1.0}_{-0.6}$	-60^{+32}_{-32}	275^{+73}_{-72}
Si XIII	$4.0^{+0.4}_{-0.4}$	-123^{+39}_{-45}	314^{+116}_{-50}
S XVI	66^{+48}_{-31}	-89^{+68}_{-48}	16^{+355}_{-16}
S XV	$4.5^{+0.1}_{-2.2}$	49^{+0}_{-105}	64^{+18}_{-0}
Fe XXIV	$3.2^{+42.9}_{-0.9}$	50^{+37}_{-37}	66^{+70}_{-31}
Fe XXIII	$1.1^{+0.4}_{-0.4}$	93^{+47}_{-63}	70^{+90}_{-39}
Fe XXII	$1.2^{+0.3}_{-0.3}$	-12^{+37}_{-29}	120^{+36}_{-44}
Fe XXI	$1.1^{+0.1}_{-0.2}$	-139^{+45}_{-50}	232^{+55}_{-53}
Fe XIX	$1.1^{+0.1}_{-0.3}$	-34^{+70}_{-87}	219^{+81}_{-67}
Fe XVIII	$0.2^{+0.2}_{-0.1}$	-52^{+90}_{-86}	83^{+108}_{-66}
Fe XVII	$0.4^{+0.2}_{-0.2}$	-110^{+55}_{-24}	6^{+3}_{-6}

Fitting the series of all species with a line series model based on the curve of growth and assuming Voigt profiles for the line shapes, shows in general only small systematic velocities.
Note that lower ionized species tend to have larger blueshifts, as expected from the ionization structure of the Strömgren sphere around the black hole.
This result is consistent with the analysis of UV data of Gies et al. (2008; ArXiv: 0801.4286).

Broad Iron Line

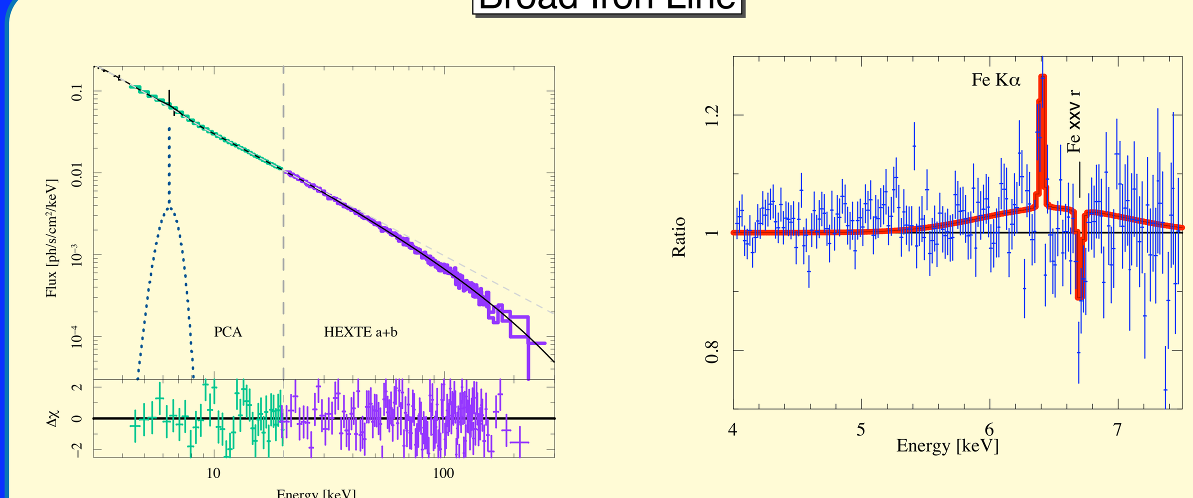

In the analysis of the *RXTE*-data a broad Fe Kα feature is found, which *can not* be explained by the narrow Fe Kα line seen with *Chandra* alone, but rather is a blend of the narrow line and a broad component such as a relativistic line. Note that the broad feature *is consistent* with the *Chandra* data, although it is difficult to see due to the high resolution of the HETGS.